

# Bow shocks, bow waves, and dust waves. I. Strong coupling limit

William J. Henney & S. J. Arthur

*Instituto de Radioastronomía y Astrofísica, Universidad Nacional Autónoma de México, Apartado Postal 3-72, 58090 Morelia, Michoacán, México*

Accepted XXX. Received YYY; in original form ZZZ

## ABSTRACT

Dust waves and bow waves result from the action of a star’s radiation pressure on a stream of dusty plasma that flows past it. They are an alternative mechanism to hydrodynamic bow shocks for explaining the curved arcs of infrared emission seen around some stars. When gas and grains are perfectly coupled, for a broad class of stellar parameters, wind-supported bow shocks predominate when the ambient density is below  $100\text{ cm}^{-3}$ . At higher densities radiation-supported bows can form, tending to be optically thin bow waves around B stars, or optically thick bow shocks around early O stars. For OB stars with particularly weak stellar winds, radiation-supported bows become more prevalent.

**Key words:** circumstellar matter – radiation: dynamics – stars: winds, outflows

## 1 INTRODUCTION

Curved emission arcs around stars (e.g., Gull & Sofia 1979) are often interpreted as *bow shocks*, due to a supersonic hydrodynamic interaction between the star’s wind and an external stream. This stream may be due to the star’s own motion or to an independent flow, such as an H II region in the champagne phase (Tenorio-Tagle 1979), or another star’s wind (Canto et al. 1996). However, an alternative interpretation in some cases may be a radiation-pressure driven bow wave, as first proposed by van Buren & McCray (1988, §vi). In this scenario (see Fig. 1), photons emitted by the star are absorbed by dust grains in the incoming stream, with the resultant momentum transfer being sufficient to decelerate and deflect the grains within a certain distance from the star, forming a dust-free, bow-shaped cavity with an enhanced dust density at its edge.

Two regimes are possible, depending on the strength of coupling between the gas (or plasma) and the dust. In the strong-coupling regime, gas–grain drag decelerates the gas along with the dust. If the stream is optically thin to the star’s ultraviolet radiation, then the deceleration occurs gradually over a range of radii, forming a relatively thick shell. On the other hand, if the stream is optically thick, then a shocked gas shell forms in a similar fashion to the wind-driven bow shock case, except internally supported by trapped radiation instead of shocked stellar wind. In the weak-coupling regime, the gas stream is relatively unaffected and the dust temporarily decouples to form a dust-only shell. This second case has recently been studied in detail in the context of the interaction of late O-type stars (some of which have very weak stellar winds) with dusty photoevaporation flows inside H II regions (Ochsendorf et al. 2014b,a; Ochsendorf & Tielens 2015). We follow the nomenclature proposed by Ochsendorf et al. (2014a), in which *dust wave* refers to the weak coupling case and *bow wave* to the strong coupling case. More complex, hybrid scenarios are also possible, such as that studied by van Marle et al. (2011), where a hydrodynamic bow shock forms, but the larger

dust grains that accompany the stellar wind pass right through the shocked gas shell, and form their own dust wave at a larger radius.

This is the first in a series of papers where we develop simple physical models to show in detail when and how these different interaction regimes apply when varying the parameters of the star, the dust grains, and the ambient stream. We concentrate primarily on the case of luminous early type stars, where dust is present only in the ambient stream, and not in the stellar wind. In this first paper, we consider the case where the grains are perfectly coupled to the gas via collisions. The following two papers consider the decoupling of grains and gas in a sufficiently strong radiation field (Henney & Arthur 2019a, Paper II), and how observations can distinguish between different classes of bow (Henney & Arthur 2019b, Paper III). The paper is organized as follows. In § 2 we propose a simple model for stellar bows and investigate the relative importance of wind and radiation in providing internal support for the bow shell as a function of the density and velocity of the ambient stream, and for different types of star. In § 3 we calculate the physical state of the bow shell, considering under what circumstances it can trap within itself the star’s ionization front and how efficient radiative cooling will be. In § ?? we briefly discuss the application of our models to observed bows. In § ?? we summarise the conclusions of our study.

## 2 A SIMPLE MODEL FOR STELLAR BOWS

We consider the canonical case of a bow around a star of bolometric luminosity,  $L$ , with a radiatively driven wind, which is immersed in an external stream of gas and dust with density,  $\rho$ , and velocity,  $v$ . The size and shape of the bow is determined by a generalized balance of pressure (or, equivalently, momentum) between internal and external sources. We assume that the stream is supersonic and super-alfvenic, so that the external pressure is dominated by the ram pressure,  $\rho v^2$ , and that dust grains and gas are perfectly coupled by collisions (the breakdown of this assumption is the topic of Paper II).

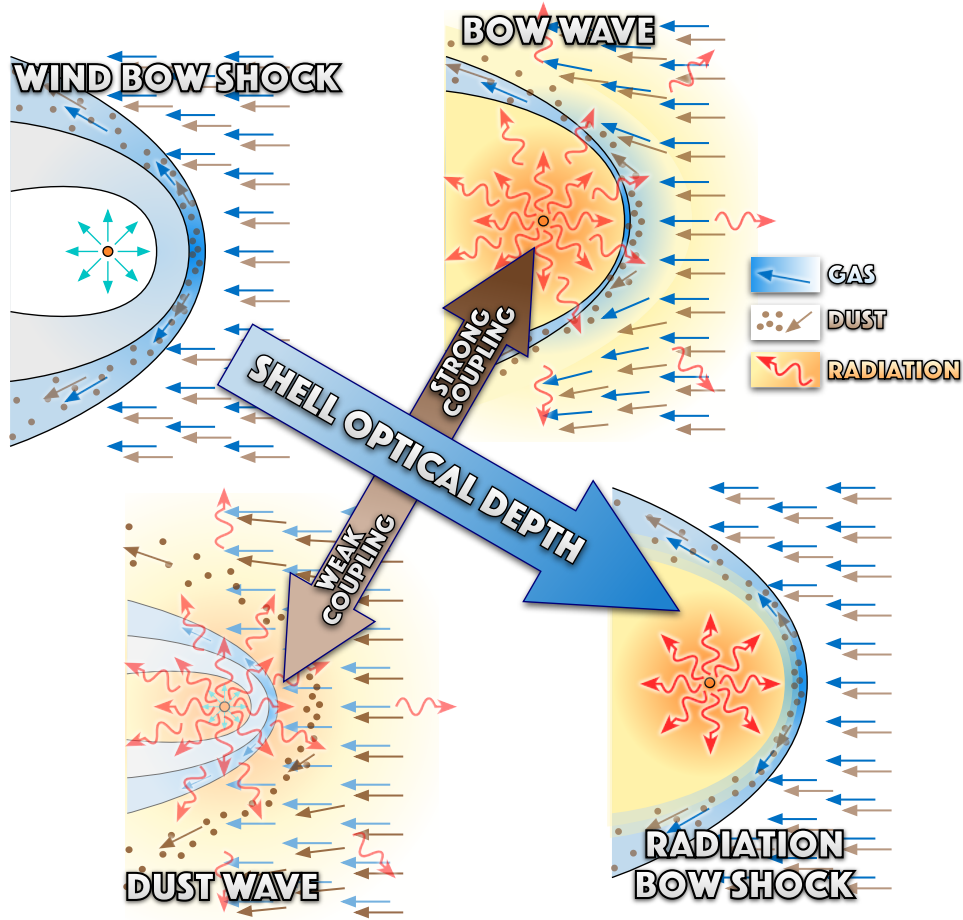


**Figure 1.** Regimes in the supersonic interaction of a luminous star with its environment. When radiation effects are unimportant, we have the standard (magneto-)hydrodynamical wind-supported bow shock (upper left), where the ram pressure of the stellar wind balances the ram pressure of the oncoming stream. As the optical depth of the shocked shell increases, the stellar radiation momentum adds to the wind ram pressure to help support the bow. If the shell is completely opaque to stellar radiation, we have a radiation-supported bow shock (lower right), where it is the stellar radiation pressure that balances the ram pressure of the external stream. For intermediate optical depths, we have two cases depending on the strength of coupling between grains and gas. If the coupling is strong, then we have a radiation-supported bow wave (upper right), where the plasma stream as a whole is gradually radiatively decelerated as it approaches the star. If the coupling is weak, then the radiation momentum is felt only by the dust, which decouples from the gas to form a dust wave, with the gas stream continuing inward to form a wind-supported bow shock closer to the star. Note that the gas–grain coupling is both direct (via collisions) and indirect (via the magnetic field) (see Paper II).

Although dust grains typically constitute only a small fraction  $Z_d \sim 0.01$  of the mass of the external stream, they nevertheless dominate the broad-band opacity at FUV, optical and IR wavelengths if they are present.<sup>1</sup> The strong coupling assumption means that all the radiative forces applied to the dust grains are directly felt by the gas also.

## 2.1 Bows supported by radiation and wind

The internal pressure is the sum of wind ram pressure and the effective radiation pressure that acts on the bow shell. The radiative momentum loss rate of the star is  $L/c$  and the wind momentum loss rate can be expressed as

$$\dot{M}V = \eta_w L/c, \quad (1)$$

where  $\eta_w$  is the momentum efficiency of the wind, which is typically  $< 1$  (Lamers & Cassinelli 1999). If the optical depth is very large, then all of the stellar radiative momentum, emitted with rate  $L/c$ , is trapped by the bow shell. In the single scattering limit,<sup>2</sup> and

<sup>1</sup> At EUV wavelengths ( $\lambda < 912 \text{ \AA}$ ), gas opacity dominates if the hydrogen neutral fraction is larger than  $\approx 0.001$ , see discussion of ionization front trapping below.

<sup>2</sup> Although it may seem inconsistent to assume single scattering in the case of high optical depths, this is defensible for the following reasons.

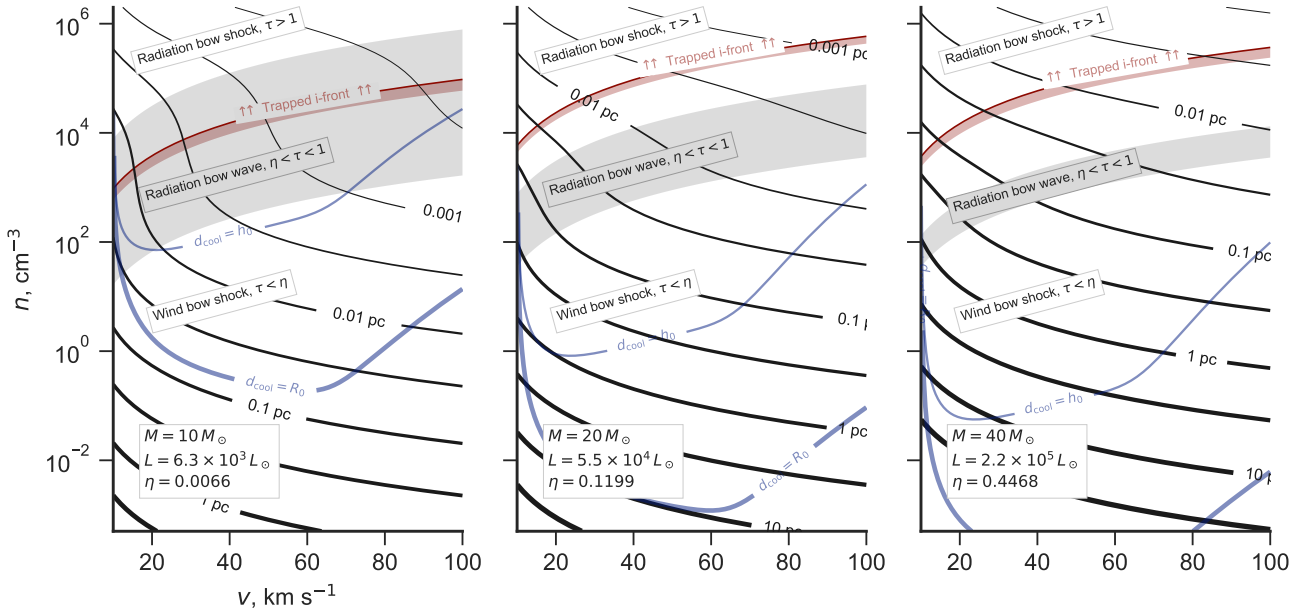


**Figure 2.** Bow regimes in parameter space ( $v, n$ ) of the external stream for main-sequence OB stars of different masses: (a)  $10 M_{\odot}$ , (b)  $20 M_{\odot}$ , (c)  $40 M_{\odot}$ . In all cases,  $\kappa = 600 \text{ cm}^2 \text{ g}^{-1}$  and efficient gas-grain coupling is assumed. Solid black lines of varying width show the bow size (star-apex separation,  $R_0$ ), while gray shading shows the radiation bow wave regime, with lower border  $\tau = \eta_w$  and upper border  $\tau = 1$ , where  $\tau = 2\kappa\rho R_0$  is the optical depth through the bow. For bows above the red solid line, the ionization front is trapped inside the bow (§ 3.1). Blue lines delineate different cooling regimes (§ 3.2). Above the thin blue line ( $d_{\text{cool}} = h_0$ ), the bow shock radiates efficiently, forming a thin shocked shell. Below the thick blue line ( $d_{\text{cool}} = R_0$ ), the bow shock is essentially non-radiative.

temporarily neglecting the wind for clarity of exposition, then pressure balance at the bow apex, a distance  $R_0$  along the symmetry axis from the star is given by

$$\frac{L}{4\pi c R_0^2} = \rho v^2, \quad (2)$$

which yields a fiducial bow shock radius in this optically thick, radiation-only limit as

$$R_* = \left( \frac{L}{4\pi c \rho v^2} \right)^{1/2}. \quad (3)$$

We now consider the opposite, optically thin limit. If the total opacity (gas plus dust) per total mass (gas plus dust) is  $\kappa$  (with units of  $\text{cm}^2 \text{ g}^{-1}$ ), then the radiative acceleration is

$$a_{\text{rad}} = \frac{\kappa L}{4\pi c R^2}. \quad (4)$$

Therefore, an incoming stream with initial velocity,  $v_{\infty}$ , can be brought to rest by radiation alone at a distance  $R_{**}$  where

$$\int_{R_{**}}^{\infty} a_{\text{rad}} dr = \frac{1}{2} v_{\infty}^2, \quad (5)$$

yielding

$$R_{**} = \frac{\kappa L}{2\pi c v_{\infty}^2}. \quad (6)$$

(1) The grain albedo is not that high (typically  $\sim 0.5$  at ultraviolet through optical wavelengths). (2) The scattered radiation field is more isotropic than the stellar field, leading to cancellation in the radiative flux. (3) Absorbed radiation is re-emitted at infrared wavelengths, where the dust opacity is very much lower.

On the other hand, we can also argue as in the optically thick case above by approximating the bow shell as a surface, and balancing stellar radiation pressure against the ram pressure of the incoming stream. The important difference when the shell is not optically thick is that only a fraction  $1 - e^{-\tau}$  of the radiative momentum is absorbed by the bow, so that equation (2) is replaced with

$$\frac{L(1 - e^{-\tau})}{4\pi c R_0^2} = \rho v^2. \quad (7)$$

In the optically thin limit,  $1 - e^{-\tau} \approx \tau$ , so these two descriptions can be seen to agree ( $R_0 \rightarrow R_{**}$ ) so long as

$$\tau = 2\kappa\rho R_0, \quad (8)$$

which we will assume to hold generally.

Then, defining a fiducial optical depth,

$$\tau_* = \rho\kappa R_*, \quad (9)$$

and now reinstating the stellar wind ram pressure term from equation (1), we find that the general bow radius can be written in terms of the fiducial radius as

$$R_0 = x R_*, \quad (10)$$

where  $x$  is the solution of

$$x^2 - (1 - e^{-2\tau_* x}) - \eta_w = 0. \quad (11)$$

Since this is a transcendental equation,  $x$  must be found numerically, but we can write explicit expressions for three limiting cases:

$$x \approx \begin{cases} \text{if } \tau_* \gg 1: & (1 + \eta_w)^{1/2} \\ \text{if } \tau_*^2 \ll 1: & \tau_* + (\tau_*^2 + \eta_w)^{1/2} \approx \begin{cases} \text{if } \tau_*^2 \gg \eta_w: & 2\tau_* \\ \text{if } \tau_*^2 \ll \eta_w: & \eta_w^{1/2} \end{cases} \end{cases} \quad (12)$$

The first case,  $x \approx (1 + \eta_w)^{1/2}$ , corresponds to a *radiation bow shock* (RBS); the second case,  $x \approx 2\tau_*$ , corresponds to a *radiation bow wave* (RBW); and the third case,  $x \approx \eta_w^{1/2}$ , corresponds to a *wind bow shock* (WBS). The two bow shock cases are similar in that the external stream is oblivious to the presence of the star until it suddenly hits the bow shock shell, differing only in whether it is radiation or wind that is providing the internal pressure. In the intermediate bow wave case, on the other hand, the external stream is gradually decelerated by absorption of photons as it approaches the bow.<sup>3</sup>

## 2.2 Dependence on stellar type

We now consider the application to bow shocks around main sequence OB stars, as well as cool and hot supergiants, expressing stellar and ambient parameters in terms of typical values as follows:

$$\begin{aligned}\dot{M}_{-7} &= \dot{M} / (10^{-7} M_\odot \text{ yr}^{-1}) \\ V_3 &= V / (1000 \text{ km s}^{-1}) \\ L_4 &= L / (10^4 L_\odot) \\ v_{10} &= v_\infty / (10 \text{ km s}^{-1}) \\ n &= (\rho / \bar{m}) / (1 \text{ cm}^{-3}) \\ \kappa_{600} &= \kappa / (600 \text{ cm}^2 \text{ g}^{-1}),\end{aligned}$$

where  $\bar{m}$  is the mean mass per hydrogen nucleon ( $\bar{m} \approx 1.3m_p \approx 2.17 \times 10^{-24} \text{ g}$  for solar abundances). Note that  $\kappa = 600 \text{ cm}^2 \text{ g}^{-1}$  corresponds to a cross section of  $\approx 10^{-21} \text{ cm}^2$  per hydrogen nucleon, which is typical for interstellar medium dust (Bertoldi & Draine 1996) at far ultraviolet wavelengths, where OB stars emit most of their radiation. In terms of these parameters, we can express the stellar wind momentum efficiency as

$$\eta_w = 0.495 \dot{M}_{-7} V_3 L_4^{-1} \quad (13)$$

and the fiducial radius and optical depth as

$$R_*/\text{pc} = 2.21 (L_4/n)^{1/2} v_{10}^{-1} \quad (14)$$

$$\tau_* = 0.0089 \kappa_{600} (L_4 n)^{1/2} v_{10}^{-1}. \quad (15)$$

In Figure 2, we show results for the bow size (apex distance,  $R_0$ ) as a function of the density,  $n$ , and relative velocity,  $v_\infty$ , of the external stream, with each panel corresponding to a particular star, with parameters as shown in Table 1. To facilitate comparison with previous work, we choose stellar parameters similar to those used in the hydrodynamical simulations of Meyer et al. (2014, 2016, 2017), based on stellar evolution tracks for stars of  $10 M_\odot$ ,  $20 M_\odot$  and  $40 M_\odot$  (Brott et al. 2011) and theoretical wind prescriptions (de Jager et al. 1988; Vink et al. 2000). Although the stellar parameters do evolve with time, they change relatively little during the main-sequence lifetime of several million years.<sup>4</sup> The three examples are an early B star ( $10 M_\odot$ ), a late O star ( $20 M_\odot$ ), and an early

<sup>3</sup> A shock can still form in this case, but shocked material constitutes only a small fraction of the total column density of the shell.

<sup>4</sup> Note that we have recalculated the stellar wind terminal velocities, since the values given in the Meyer et al. papers are troublingly low. We have used the prescription  $V = 2.6V_{\text{esc}}$ , where  $V_{\text{esc}} = (2GM(1 - \Gamma_e)/R)^{1/2}$  is the photospheric escape velocity, which is appropriate for strong line-driven winds with  $T_{\text{eff}} > 21000 \text{ K}$  (Lamers et al. 1995). We find velocities of  $2500 \text{ km s}^{-1}$  to  $3300 \text{ km s}^{-1}$ , which are consistent with observations and theory (Vink et al. 1999), but at least two times higher than those cited by Meyer et al. (2014).

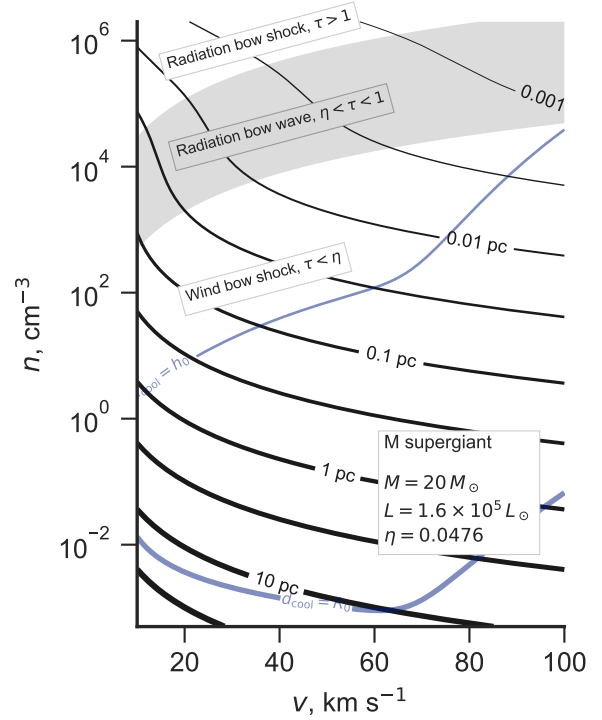


**Figure 3.** As Fig. 2, but for a cool M-type supergiant instead of hot main sequence stars. A smaller dust opacity is used,  $\kappa = 60 \text{ cm}^2 \text{ g}^{-1}$ , because of the reduced extinction efficiency at the optical/infrared wavelengths emitted by this star.

O star ( $40 M_\odot$ ), which cover the range of luminosities and wind strengths expected from bow-producing hot main sequence stars. The luminosity is a steep function of stellar mass ( $L \sim M^{2.5}$ ) and the wind mass-loss rate is a steep function of luminosity ( $\dot{M} \sim L^{2.2}$ ), which means that the wind momentum efficiency is also a steep function of mass ( $\eta_w \sim M^3$ ), approaching unity for early O stars, but falling to less than 1% for B stars.

It can be seen from Figure 2 that the onset of the radiation bow wave regime is very similar for the three main-sequence stars, occurring at  $n > 20$  to  $40 v_{10}^2$ . An important difference, however, is that for the  $40 M_\odot$  star, which has a powerful wind, the radiation bow wave regime only occurs for a very narrow range of densities, whereas for the  $10 M_\odot$  star, with a much weaker wind, the regime is much broader, extending to  $n < 10^4 v_{10}^2$ . Another difference is the size scale of the bows in this regime, which is  $R_0 = 0.001 \text{ pc}$  to  $0.003 \text{ pc}$  for the  $10 M_\odot$  star if  $v_\infty = 40 \text{ km s}^{-1}$ , but  $R_0 \approx 0.1 \text{ pc}$  for the  $40 M_\odot$  star, assuming the same inflow velocity.

Figure 3 shows results for a cool M-type supergiant star with stellar parameters inspired by Betelgeuse ( $\alpha$  Orionis), as listed in Table 1. Unlike the UV-dominated spectrum of the hot stars, this star emits predominantly in the near-infrared, where the dust extinction efficiency is lower, so we adopt a lower opacity of  $60 \text{ cm}^2 \text{ g}^{-1}$ . This has the effect of shifting the radiation bow wave regime to higher densities:  $n = 1000$  to  $30000 v_{10}^2$  in this case.

**Table 1.** Stellar parameters for example stars

	$M/M_{\odot}$	$L_4$	$\dot{M}_{-7}$	$V_3$	$\eta_w$	Sp. Type	$T_{\text{eff}}/\text{kK}$	$\lambda_{\text{eff}}/\mu\text{m}$	$S_{49}$	Figures
Main-sequence OB stars	10	0.63	0.0034	2.47	0.0066	B1.5 V	25.2	0.115	0.000 13	2a
	20	5.45	0.492	2.66	0.1199	O9 V	33.9	0.086	0.16	2b, 6
	40	22.2	5.1	3.31	0.4468	O5 V	42.5	0.068	1.41	2c
Blue supergiant star	33	30.2	20.2	0.93	0.3079	B0.7 Ia	23.5	0.123	0.016	4
Red supergiant star	20	15.6	100	0.015	0.0476	M1 Ia	3.6	0.805	0	3

### 2.3 Effects of stellar gravity

In principle, gravitational attraction from the star, of mass  $M$ , will partially counteract the radiative acceleration. This can be accounted for by replacing  $L$  with an effective luminosity

$$L_{\text{eff}} = L(1 - \Gamma_E^{-1}), \quad (16)$$

in which  $\Gamma_E$  is the Eddington factor:

$$\Gamma_E = \frac{\kappa L}{4\pi c G M} = 458.5 \frac{\kappa_{600} L_4}{M}, \quad (17)$$

where, in the last expression,  $M$  is measured in solar masses. For the stars in Table 1, we find  $\Gamma_E \approx 30$  to 400, so gravity can be safely ignored. When the optical depth of the bow is very large,  $\tau > \ln \Gamma_E \sim 5$ , gravity will exceed the radiation force in the outer parts of the shell (see Rodríguez-Ramírez & Raga 2016), but it is generally too weak to effect the shell structure even in such a case, see § 3.3 below.

## 3 PHYSICAL STATE OF THE BOW SHELL

There are two shocked zones in the bow: an inner zone of shocked stellar wind, and an outer zone of decelerated ambient stream. For OB stars, dust grains are present only in the ambient stream, whereas for cool stars they will also be present in the stellar wind. In the remainder of this paper, we will concentrate on the OB star case, where it is the outer zone that is most important observationally. Bows are typically detected via their infrared radiation (absorption and re-emission by dust of stellar radiation), or by emission lines such as the hydrogen  $H\alpha$  line.

### 3.1 Ionization state

In this section we calculate whether the star is capable of photoionizing the entire bow shock shell, or whether the recombination front will be trapped within it. The number of hydrogen recombinations<sup>5</sup> per unit time per unit area in a fully ionized shell is

$$\mathcal{R} = \alpha_B n_{\text{sh}}^2 h_{\text{sh}}, \quad (18)$$

while the advective flux of hydrogen nuclei through the shock is

$$\mathcal{A} = n v, \quad (19)$$

and the flux of hydrogen-ionizing photons ( $h\nu > 13.6\text{ eV}$ ) incident on the inner edge of the shell is

$$\mathcal{F} = \frac{S}{4\pi R_0^2}, \quad (20)$$

<sup>5</sup> The diffuse field is treated in the on-the-spot approximation, assuming all emitted Lyman continuum photons are immediately re-absorbed locally, so the case B recombination co-efficient,  $\alpha_B = 2.6 \times 10^{-13} T_4^{-0.7} \text{ cm}^3 \text{ s}^{-1}$ , is used, where  $T_4 = T/10^4 \text{ K}$ .

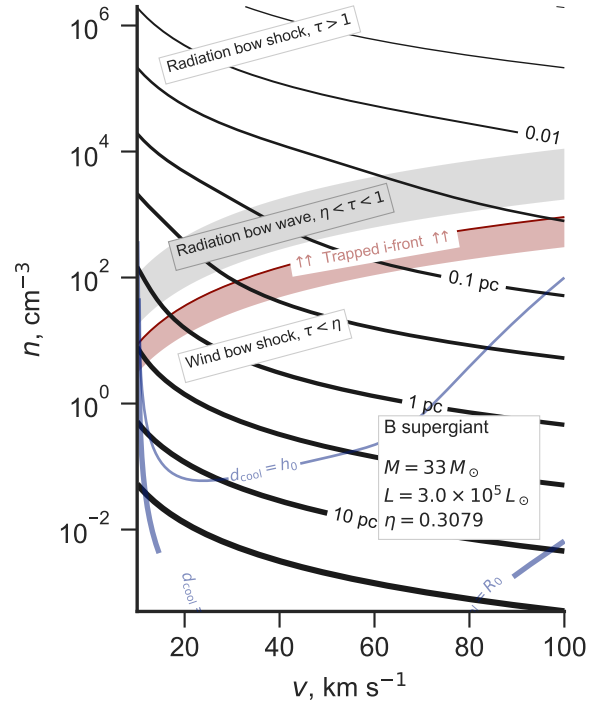


**Figure 4.** As Fig. 2, but for an evolved B-type supergiant instead of main sequence stars. This is similar to the early O MS star of Fig. 2c in many respects, except for the trapping of the ionization front, which occurs for much lower outer stream densities.

where  $S$  is the ionizing photon luminosity of the star. Any shell with  $\mathcal{R} + \mathcal{A} > \mathcal{F}$  cannot be entirely photoionized by the star, and so must have trapped the ionization front.

The ratio of advective particle flux to ionizing flux is, from equations (3), (19), (20),

$$\frac{\mathcal{A}}{\mathcal{F}} = 5.86 \times 10^{-5} \frac{x^2 L_4}{v_{10} S_{49}}, \quad (21)$$

where

$$S_{49} = S/(10^{49} \text{ s}^{-1}).$$

Numerical values of  $S_{49}$  for our three example stars are given in Table 1, taken from Figure 4 of Sternberg et al. (2003). Since  $\mathcal{A} \ll \mathcal{F}$  in nearly all cases, for clarity of exposition we ignore  $\mathcal{A}$  in the following discussion, although it is included in quantitative calculations. The column density of the shocked shell can be found, for example, from equations (10) and (12) of Wilkin (1996) in the



limit  $v_\infty/V \rightarrow 0$  (Wilkin's parameter  $\alpha$ ) and  $\theta \rightarrow 0$ . This yields

$$n_{\text{sh}} h_{\text{sh}} = \frac{3}{4} n R_0. \quad (22)$$

Assuming strong cooling behind the shock,<sup>6</sup> the shell density is

$$n_{\text{sh}} = \mathcal{M}_0^2 n \quad (23)$$

where  $\mathcal{M}_0 = v_\infty/c_s$  is the isothermal Mach number of the external stream.<sup>7</sup> Putting these together with equations (3) and (9), one finds that  $\mathcal{R} > \mathcal{F}$  implies

$$x^3 \tau_* > \frac{4 S c c_s \bar{m}^2 \kappa}{3 \alpha L}. \quad (24)$$

From equation (11), it can be seen that  $x$  depends on the external stream parameters,  $n$ ,  $v_\infty$  only via  $\tau_*$ , and so equation (24) is a condition for  $\tau_*$ , which, by using equation (15), becomes a condition on  $n/v_{10}^2$ . In the radiation bow shock case,  $x = (1 + \eta_w)^{1/2}$ , and the condition can be written:

$$\text{RBS: } \frac{n}{v_{10}^2} > 2.65 \times 10^8 \frac{S_{49}^2 T_4^{3.4}}{L_4^3 (1 + \eta_w)^3}. \quad (25)$$

In the radiation bow wave case,  $x = 2\tau_*$ , and the condition can be written:

$$\text{RBW: } \frac{n}{v_{10}^2} > 5.36 \times 10^4 \frac{S_{49}^{1/2} T_4^{0.85}}{\kappa_{600}^{3/2} L_4^{3/2}}. \quad (26)$$

In the wind bow shock case, the result is the same as equation (25), but changing the factor  $(1 + \eta_w)^3$  to  $\eta_w^3$ . For the example hot stars in Table 1, and assuming  $\kappa_{600} = 1$ ,  $T_4 = 0.8$ , the resulting density threshold is  $n > (1000 \text{ to } 5000) v_{10}^2$ , depending only weakly on the stellar parameters, which is shown by the red lines in Figure 2. For the  $10 M_\odot$  star, this is in the radiation bow wave regime, whereas for the higher mass stars it is in the radiation bow shock regime. When the external stream is denser than this, then the outer parts of the shocked shell may be neutral instead of ionized, giving rise to a cometary compact H II region (Mac Low et al. 1991; Arthur & Hoare 2006). This is only necessarily true, however, when the star is isolated. If the star is in a cluster environment, then the contribution of other nearby massive stars to the ionizing radiation field must be considered.

Quite different results are obtained for a B-type supergiant star (see Tab. 1 and Fig. 4), which has a similar bolometric luminosity and wind strength to the  $40 M_\odot$  main-sequence star, but a hundred times lower ionizing luminosity. This results in a far lower threshold for trapping the ionization front of  $n > 40 v_{10}^2$ . The advective flux,  $\mathcal{A}$ , is relatively stronger for this star than for the main-sequence stars, but even for  $v_{10} < 2$ , where the effect is strongest, the change is only of order the width of the dark red line in Figure 4.

In principle, when the ionization front trapping occurs in the bow wave regime, then the curves for  $R_0$  will be modified in the region above the red line because all of the ionizing radiation is trapped in the shell due to gas opacity, which is not included in equation (8). However, this only happens for our  $10 M_\odot$  star, which has a relatively soft spectrum. Table 1 gives the peak wavelength of the stellar spectrum for this star as  $\lambda_{\text{eff}} = 0.115 \mu\text{m}$ , which

is significantly larger than the hydrogen ionization threshold at  $0.0912 \mu\text{m}$ , meaning that only a small fraction of the total stellar luminosity is in the EUV band and affected by the gas opacity. The effect on  $R_0$  is therefore small. For the higher mass stars,  $\lambda_{\text{eff}} < 0.0912 \mu\text{m}$ , so the majority of the luminosity is in the EUV band, but in these cases the ionization front trapping occurs well inside the radiation bow shock zone, where the dust optical depth is already sufficient to trap all of the radiative momentum.

### 3.2 Efficiency of radiative cooling

In this section, we calculate whether the radiative cooling is sufficiently rapid behind the bow shock to allow the formation of a thin, dense shell. In general, cooling is least efficient at low densities, so we will assume that the wind bow shock regime applies unless otherwise specified. We label quantities just outside the shock by the subscript “0”, quantities just inside the shock (after thermalization, but before any radiative cooling) by the subscript “1”, and quantities after the gas has cooled back to the photoionization equilibrium temperature by the subscript “2”. Assuming a ratio of specific heats,  $\gamma = 5/3$ , the relation between the pre-shock and immediate post-shock quantities is

$$\frac{n_1}{n_0} = \frac{4\mathcal{M}_0^2}{\mathcal{M}_0^2 + 3} \quad (27)$$

$$\frac{T_1}{T_0} = \frac{1}{16} (5\mathcal{M}_0^2 - 1) (1 + 3/\mathcal{M}_0^2) \quad (28)$$

$$\frac{v_1}{v_0} = \left( \frac{n_1}{n_0} \right)^{-1}, \quad (29)$$

where  $\mathcal{M}_0 = v_0/c_s$ . The cooling length of the post-shock gas can be written as

$$d_{\text{cool}} = \frac{3P_1 v_1}{2(\mathcal{L}_1 - \mathcal{G}_1)}, \quad (30)$$

where  $P_1$  is the thermal pressure and  $\mathcal{L}_1$ ,  $\mathcal{G}_1$  are the volumetric radiative cooling and heating rates. For fully photoionized gas, we have  $P_1 \approx 2n_1 k T_1$ ,  $\mathcal{L}_1 = n_1^2 \Lambda(T_1)$ , and  $\mathcal{G}_1 = n_1^2 \Gamma(T_1)$ , where  $\Lambda(T)$  is the cooling coefficient, which is dominated by metal emission lines that are excited by electron collisions, and  $\Gamma(T)$  is the heating coefficient, which is dominated by hydrogen photo-electrons (Osterbrock & Ferland 2006). The cooling coefficient has a maximum around  $10^5 \text{ K}$ , and for typical ISM abundances can be approximated as follows:

$$\Lambda_{\text{warm}} = 3.3 \times 10^{-24} T_4^{2.3} \text{ erg cm}^3 \text{ s}^{-1} \quad (31)$$

$$\Lambda_{\text{hot}} = 10^{-20} T_4^{-1} \text{ erg cm}^3 \text{ s}^{-1} \quad (32)$$

$$\Lambda = \left( \Lambda_{\text{warm}}^{-k} + \Lambda_{\text{hot}}^{-k} \right)^{-1/k} \quad \text{with } k = 3, \quad (33)$$

which is valid in the range  $0.7 < T_4 < 1000$ . We approximate the heating coefficient as

$$\Gamma = 1.77 \times 10^{-24} T_4^{-1/2} \text{ erg cm}^3 \text{ s}^{-1}, \quad (34)$$

where the coefficient is chosen so as to give  $\Gamma = \Lambda$  at an equilibrium temperature of  $T_4 = 0.8$ .

In Figure 2 we show curves calculated from equations (27) to (34), corresponding to  $d_{\text{cool}} = R_0$  (thick blue line) and  $d_{\text{cool}} = h_0$  (thin blue line), where  $h_0$  is the shell thickness in the limit of instantaneous cooling. In this context,  $n_0 = n$  and  $n_2 = n_{\text{sh}}$ , so that  $h_0$  follows from equations (22) and (23) as

$$h_0 = \frac{3}{4} \mathcal{M}_0^{-2} R_0. \quad (35)$$

<sup>6</sup> This is shown to be justified in § 3.2.

<sup>7</sup> The sound speed depends on the temperature and hydrogen and helium ionization fractions,  $y$  and  $y_{\text{He}}$  as  $c_s^2 = (1 + y + z_{\text{He}} y_{\text{He}}) (kT/\bar{m})$ , where  $z_{\text{He}}$  is the helium nucleon abundance by number relative to hydrogen and  $k = 1.3806503 \times 10^{-16} \text{ erg K}^{-1}$  is Boltzmann's constant. We assume  $y = 1$ ,  $y_{\text{He}} = 0.5$ ,  $z_{\text{He}} = 0.09$ , so that  $c_s = 11.4 T_4^{1/2} \text{ km s}^{-1}$ .

The bends in the curves at  $v \approx 50 \text{ km s}^{-1}$  are due to the maximum in the cooling coefficient  $\Lambda(T)$  around  $10^5 \text{ K}$ . For bows with outer stream densities above the thin blue line, radiative cooling is so efficient that the bow shock can be considered isothermal, and so the shell is dense and thin (at least, in the apex region). It can be seen that the ionization front trapping always occurs at densities larger than this, which justifies the use of equation (23) in the previous section. For bows with outer stream densities below the thick blue line, cooling is unimportant and the bow shock can be considered non-radiative. In this case the shell is thicker than in the radiative case,  $h_{\text{sh}}/R_0 \approx 0.2$  to  $0.3$ .<sup>8</sup> For bows with outer stream densities between the two blue lines, cooling does occur, albeit inefficiently, so that the shell thickness is set by  $d_{\text{cool}}$  rather than  $h_0$ .

### 3.3 Axial structure of bow shells

In the shell of a wind-supported bow shock, the gas density is highest at the contact discontinuity, but this is no longer true for radiation-supported bows, as illustrated in Figure 5, where we schematically show the shell structure for the three cases: WBS, RBW, and RBS. In all cases, we assume a far-field mach number of  $M_\infty = 3$  for the incident stream of density  $n_\infty$ . For the WBS case (Fig. 5a), the stream is unchanged until it reaches the shock, so  $M_0 = M_\infty$  and  $n_0 = n_\infty$ . The density increases to  $n_1 = 3n_0$  in the shock (eq. [27]), and then to  $n_2 = 9n_0$  (eq. [23]) after it has cooled back down to the equilibrium photoionized temperature. In the figure, we show the case where  $d_{\text{cool}} < h_0$ , so that most of the shell is at roughly constant density. Note that although the mass flux along the axis,  $nv$ , is approximately conserved in most of the flow, this is no longer true close to the contact discontinuity, since the streamlines bend away from the axis due to lateral pressure gradients. This is what allows  $v$  to tend to zero, while  $n$  remains constant. The thermal pressure in the shocked stellar wind is equal to the shell pressure, but its density is much smaller due to a temperature that is higher by a factor of  $\approx 3100v_3^2$ , (eq. [28], assuming inefficient cooling).

For the optically thin RBW case (Fig. 5b), equations (4) to (6) can be combined to give the radial dependence of the stream velocity as it approaches the star:

$$v(R) = \left(1 - \frac{R_{**}}{R}\right)^{1/2} v_\infty. \quad (36)$$

This ballistic approximation (shown by the dashed red line in Fig. 5b) predicts that the velocity smoothly decreases to zero at  $R = R_{**}$ . However, although this is valid in the limit of high Mach number, it ignores the effects of gas pressure and so becomes invalid once the stream velocity falls close to the sound speed. The situation bears similarities to the flow in a supersonic diffuser, such as the inlet of a ramjet or other supersonic aircraft engine (Seddon & Goldsmith 1999), which slows supersonic airflow down to subsonic speeds before combustion. Exactly the opposite flow configuration is present in a rocket nozzle (Courant & Friedrichs 1948), where the flow can smoothly pass from subsonic to supersonic velocities at the throat of the nozzle. An analogy between an isothermal stellar wind and a rocket nozzle is developed in detail in § 3.5 of Lamers & Cassinelli (1999). However, in the reverse case of a supersonic diffuser, a smooth transition from supersonic to subsonic flow is not

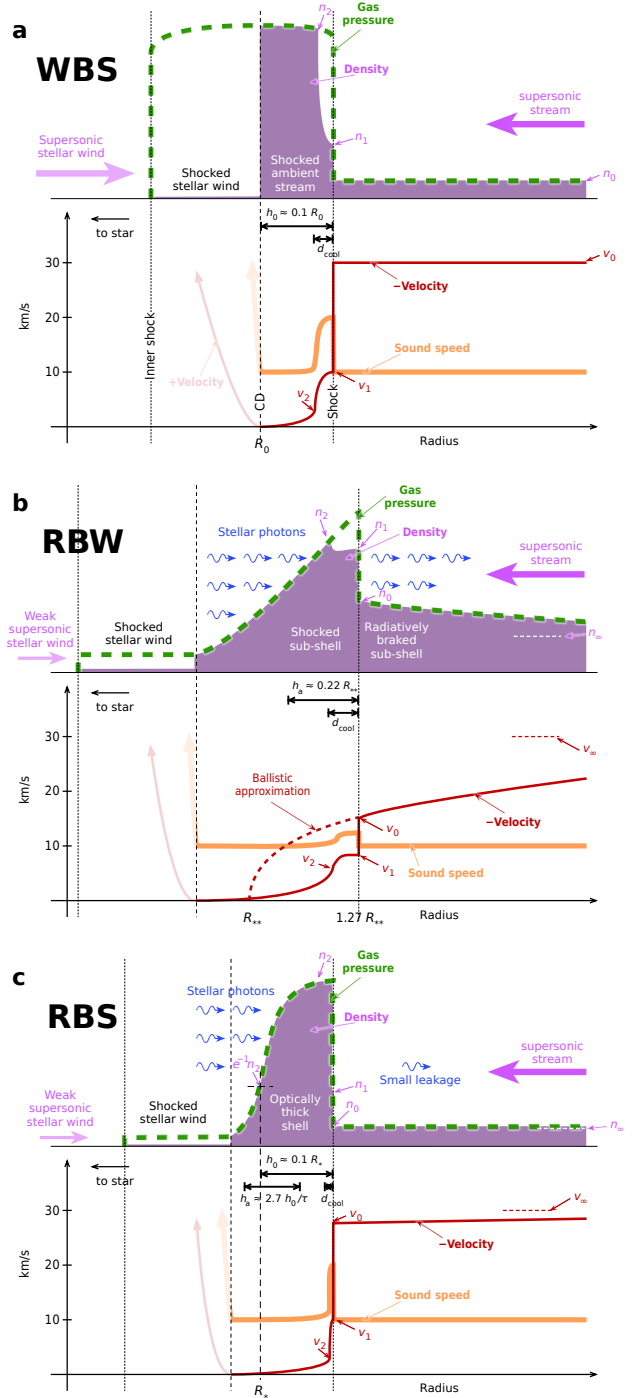


**Figure 5.** Profiles of physical variables along the axis of bow shells for (a) wind-supported bow shock; (b) radiation-supported bow wave, and (c) radiation-supported bow shock. In all cases, a stream velocity of  $30 \text{ km s}^{-1}$  and an equilibrium ionized sound speed of  $10 \text{ km s}^{-1}$  are assumed.

<sup>8</sup> An approximate value can be found from equation (22) by substituting  $n = n_0$  and  $n_{\text{sh}} \approx n_1$ , then using equation (27). Consideration of the slight increase in density between the shock and the contact/tangential discontinuity reduces this value by 5–10%.

possible (Morawetz 1956). Instead, a normal shock wave develops, which decelerates the supersonically entering flow, allowing it to exit subsonically (Embid et al. 1984; Hafez & Guo 1999). The supersonic inlet/bow wave analogy is not so exact as the rocket nozzle/stellar wind analogy due to the multi-dimensional nature of the bow shell, which means that lateral flows of gas away from the apex become

important when the velocity is subsonic.<sup>9</sup> Nonetheless, we expect that a normal shock must be present in the flow, although there does not seem to be any simple argument for predicting the exact Mach number where it will occur. In Figure. 5b, we assume that the shock occurs at a Mach number  $M_0 = 1.5$ , but multidimensional numerical simulations are necessary to test this supposition.

The shell in the RBW case therefore consists of two parts: an outer radiatively braked sub-shell, and an inner shocked sub-shell. In the outer sub-shell, the density gradually increases inwards as the stream is decelerated by the absorbed photons, reaching

$$n_0 = \frac{M_\infty}{M_0} n_\infty \quad (37)$$

just outside the shock ( $n_0 = 2n_\infty$  for the case illustrated). In the inner sub-shell, on the other hand, the pressure must increase outwards, since it is subsonic and therefore in approximate hydrostatic equilibrium with an outward-pointing effective gravity from the radiation force. The shell thickness will be set by the hydrostatic scale height,  $h_a = c_s^2/a_{\text{rad}}$ , which by eqs. (4, 6) is given by

$$h_a = \frac{2R_{**}}{M_\infty^2}. \quad (38)$$

If the cooling is efficient ( $d_{\text{cool}} < h_a$ ), then most of the sub-shell is isothermal and the density will fall off exponentially towards the star. The contact discontinuity with the stellar wind will form at the point where the shell pressure has fallen by a factor of order  $\tau/\eta_w$ , but this has no influence on the bulk of the shell, which is pressurized by radiation, not wind. If, as we suspect,  $M_0$  depends only weakly, if at all, on  $M_\infty$ , then eqs. (37, 38) imply that the inner shocked sub-shell represents a fraction  $\approx M_\infty^{-1}$  of the total shell optical depth, which means that the outer supersonic sub-shell dominates for highly supersonic stream velocities.

For the optically thick RBS case (Fig. 5c), the shell density profile is no longer simply exponential since the pressure scale height now increases as one moves away from the star, due to the extinction-induced decline in radiation flux. Assuming single scattering and plane geometry, the resultant hydrostatic density profile is doubly exponential:

$$n(R) = n_2 e^{-e^{-x}} \quad \text{where} \quad x = n_2 \bar{m} \kappa (R - R_*). \quad (39)$$

The shell density increases from  $e^{-1}n_2$  at  $R_*$  to saturate at  $n_2$  for  $R > R_* + h_a$ , where  $h_a$  is now the pressure scale height at the inner edge of the shell. From equations (3, 6, 8, 35, 38), and taking  $R_0 \approx R_*$ , we find

$$h_a \approx \frac{4h_0}{3\tau}. \quad (40)$$

We show results for a total shell optical depth  $\tau = 3$ , for which  $h_a$  is a significant fraction of  $h_0$ . For much larger optical depths,  $h_0 \gg h_a$  so that the constant density portion of the shell will dominate the total column. A small fraction  $e^{-\tau}$  of the photons will penetrate the shell and be available to decelerate the supersonic stream, as in the RBW case, yielding  $v_0 = (1 - \tau e^{-\tau}) v_\infty$ . In the illustrated case of  $\tau = 3$ , the resultant speed reduction before the shock is only 8%. As mentioned in § 2.3, radiative acceleration becomes less important than gravity in the outer regions of an opaque shell. However, in order for this to have a significant effect on the shell,

the gravitational scale height would have to be less than the shell thickness:  $\Gamma_E h_a < h_0$ . From equation (40) this translates to  $\tau > \frac{4}{3}\Gamma_E$ , where Eddington factors are  $\Gamma_E \sim 100$  for luminous stars. Such large optical depths would require extremely high ambient densities of  $n > 2 \times 10^7 L_4 v_{10}^2 (10 M_\odot/M)^2 \text{ cm}^{-3}$ , where we have used equations (9, 17) and that  $\tau \approx 2\tau_*$  in the RBS limit.

## 4 DISCUSSION

### 4.1 Environments of bow-forming stars

The stellar bows modeled in this paper can be seen as either due to the motion of a star through the interstellar medium, or due to the motion of the interstellar medium that flows past the star. The first case corresponds to runaway stars (Blaauw 1961), which have been ejected from a binary system or stellar cluster (Hoogerwerf et al. 2001), while the second case can be due to photoevaporation and champagne flows in H II regions (Tenorio-Tagle 1979; Shu et al. 2002; Henney et al. 2005), or to general turbulent flows in the Galaxy (e.g., Ballesteros-Paredes et al. 1999). In this section, we consider the stream densities and velocities expected in each of these scenarios, and compare them with our predictions for the type of bows that should result.

Although some runaway stars have velocities exceeding  $100 \text{ km s}^{-1}$ , most are moving considerably slower, with a median peculiar velocity of about  $30 \text{ km s}^{-1}$  (Tetzlaff et al. 2011). The higher velocity runaways are likely produced by dynamical interactions in the center of young clusters (Gualandris et al. 2004), whereas the supernova-induced dissolution of binary systems is predicted to primarily produce “walkaways” with even slower velocities of order  $10 \text{ km s}^{-1}$  (Renzo et al. 2018). Environmental flows are also expected to be of order  $10 \text{ km s}^{-1}$ , which is a characteristic velocity dispersion for warm neutral gas in the inner Galaxy (Marasco et al. 2017) and also a typical expansion velocity for H I shells (Ehlerová & Palouš 2005). Internal velocity dispersions within H II regions are subsonic ( $5 \text{ km s}^{-1}$  to  $10 \text{ km s}^{-1}$ ) for small regions, such as the Orion Nebula, containing one or a few ionizing stars (Arthur et al. 2016). This increases slowly for more luminous regions as  $\sigma \propto L^{1/4}$  (Bordalo & Telles 2011), so giant star forming complexes such as Carina (100 times more luminous than Orion) show velocity dispersions of order  $20 \text{ km s}^{-1}$  (Damiani et al. 2016). Higher velocities of  $30 \text{ km s}^{-1}$  to  $40 \text{ km s}^{-1}$  are reached in divergent photoevaporation flows (Dyson 1968), but this is achieved at expense of a lower density. Given all the above, we expect there to be many more bows with relative stream velocity  $v_\infty \sim 20 \text{ km s}^{-1}$  than bows with  $v_\infty \sim 100 \text{ km s}^{-1}$ .

Turning now to the ambient density, if bow shock stars were randomly sampling the volume of the Galactic disk, then we would expect the average density to be  $< 1 \text{ cm}^{-3}$ . The dominant gas phase (Ferrière 2001) near the Galactic mid-plane is the Warm Neutral Medium with a volume filling fraction of 45% (Fig. 11 of Kalberla & Kerp 2009) and an average density of  $0.9 \text{ cm}^{-3}$  at the Solar circle (§ 4 of Kalberla & Dedes 2008). Significant fractions of the volume ( $\approx 20\%$  each) are also occupied by the Warm Ionized Medium and Hot Ionized Medium, which have even lower densities ( $\approx 0.3 \text{ cm}^{-3}$  and  $10^{-3} \text{ cm}^{-3}$ , respectively) and which increasingly dominate the volume for heights  $z > 500 \text{ pc}$  above the plane. The denser Cold Neutral Medium ( $n \approx 10 \text{ cm}^{-3}$  to  $100 \text{ cm}^{-3}$ ) and Molecular Clouds ( $n > 1000 \text{ cm}^{-3}$ ) occupy much smaller volumes ( $\approx 10\%$  and  $< 1\%$ , respectively). However, observations of stellar bows are clearly biased towards these higher densities.

In part, this bias is due to bows being easier to detect in denser

<sup>9</sup> In the aeronautical case, the inlet is usually designed so that multiple oblique shocks partially decelerate the flow before it passes through the normal shock. This is the analogy of the initial gradual radiative deceleration in the bow wave.



environments. Depending on the emission mechanism, the shell luminosity will be proportional to the column density ( $\propto nR_0$ ) or volume emission measure ( $\propto n^2 R_0^3$ ), which are both increasing functions of  $n$ .<sup>10</sup> Another contribution to the high-density bias is simply that none but the highest velocity high-mass stars can move far during their lifetime from the molecular clouds where they were born. Even a runaway star with  $v = 30 \text{ km s}^{-1}$ , will travel  $< 120 \text{ pc}$  during an O-star lifetime of  $< 4 \text{ Myr}$ , which is of the same order as the sizes of Giant Molecular Clouds. Many observed stellar bows are found in high mass star clusters associated with large H II regions (Povich et al. 2008; Sexton et al. 2015). The ionized gas density in Carina, for example, has an average value of  $\approx 100 \text{ cm}^{-3}$  (Oberst et al. 2011; Damiani et al. 2016), although with peaks  $> 3000 \text{ cm}^{-3}$  in photoevaporation flows from embedded molecular globules (Smith et al. 2004). In more compact H II regions, such as the Orion Nebula, ionized densities up to  $10^4 \text{ cm}^{-3}$  are found on scales of about  $0.1 \text{ pc}$  (Weilbacher et al. 2015; O’Dell et al. 2017).

In § 2.2 we found that the bow is wind-supported when  $\tau_*^2 < \eta_w$ , where  $\tau_*$  is a fiducial optical depth (eq. [15]) and  $\eta_w$  is the radiative momentum efficiency of the stellar wind (eq. [13]). This translates into a maximum stream density for wind-supported bows of

$$n_{\text{max}} \approx (30 \text{ cm}^{-3}) \left( \frac{v}{10 \text{ km s}^{-1}} \right)^2 \left( \frac{\eta_w}{\eta_{\text{vink}}} \right) \left( \frac{600 \text{ cm}^2 \text{ g}^{-1}}{\kappa} \right), \quad (41)$$

which is largely insensitive to spectral type between early-B and early-O stars. In this equation, we have expressed the wind efficiency in terms of the Table 1 values,  $\eta_{\text{vink}}$ , which are calculated from the Vink et al. (1999) recipe, and the UV dust opacity in terms of the standard ISM value adopted in § 2.2.

Therefore, runaway stars moving through the diffuse ISM with  $n \sim 1 \text{ cm}^{-3}$  and  $v \sim 30 \text{ km s}^{-1}$  are safely in the WBS regime, having  $n \approx 0.004 n_{\text{max}}$  for the default wind and dust parameters. On the other hand, slow-moving stars in H II regions of moderate density ( $n \sim 100 \text{ cm}^{-3}$ ) can easily have  $n > n_{\text{max}}$ , meaning that their bows will be radiation supported.

For cases where the stellar wind or dust properties differ from our assumed values, then these conclusions may change. For instance, there are a growing number of stars, for which very low mass-loss rates have been diagnosed from UV, optical or infrared line profiles (Martins et al. 2005; Marcolino et al. 2009; Najarro et al. 2011; Martins et al. 2012; Smith et al. 2017). Most of these stars are late-type O dwarfs, for which the Vink et al. (2000) prescription predicts a mass-loss rate of  $3 \times 10^{-8}$  to  $10^{-7} M_{\odot} \text{ yr}^{-1}$ , whereas the observed values are in the range  $10^{-10}$  to  $3 \times 10^{-9} M_{\odot} \text{ yr}^{-1}$  – a shortfall of 10 to 1000! This “weak wind problem” is a far larger discrepancy than can be explained by clumping effects. A potential (partial) resolution is to suppose that internal shocks near the base of the wind heat a large fraction of the gas to coronal temperatures, where it is no longer detectable by means of standard wind diagnostic lines (Lucy 2012). However, in cases where x-ray diagnostics have been used to trace the mass loss this hot component ( $\mu \text{ Col}$ , Huenemoerder et al. 2012;  $\zeta \text{ Oph}$ , Cohen et al. 2014), rates that are an order of magnitude below the Vink values are still found. We therefore show in

## 4.2 Impact of the weak-wind phenomenon

Hot stars, comparison with expected velocities and densities.

Expected velocities. There are cases of high velocities, e.g.,

<sup>10</sup> From § 2.1, the bow size falls relatively slowly as  $R_0 \propto n^{-1/2}$  in the WBS and RBS cases, and is independent of  $n$  in the RBW case.

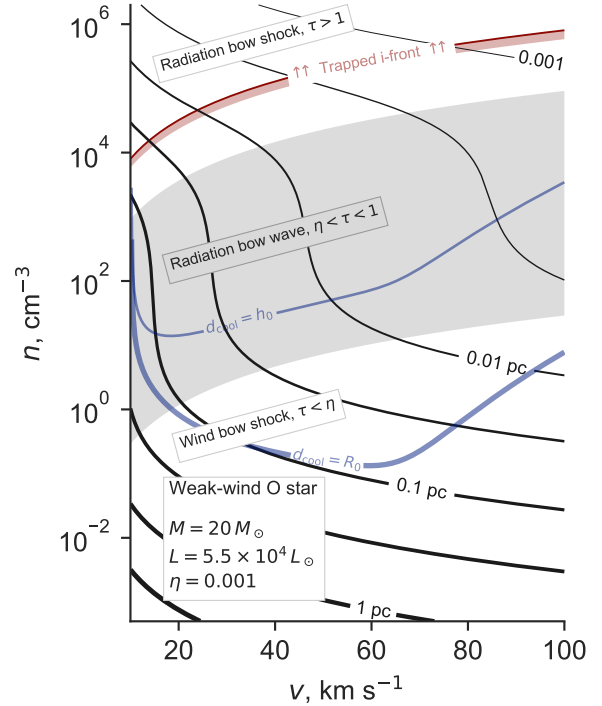


**Figure 6.** As Fig. 2, but for a weak-wind O star, similar to the sample observed by Martins et al. (2005). For this star, radiation-supported bow waves (gray shading) occur over a much larger region of parameter space than for a normal-wind star of the same spectral type (see Fig. 2b).

AE Aur, but they are probably rare. (Renzo et al. 2018) In cases, where proper motions are measured, they are often low.

Metallicity dependence of wind strength. RBW more likely at lower metallicities.

Weak wind stars - repeat the 20 Msun case, but for a much lower  $\eta_w$

Cool stars, comparison with observed densities (Betelgeuse, for instance). Other ones in (Cox et al. 2012).

Prospects for observation in LMC: 1 parsec = 4 arcsec, so need JWST to get most of them.

## 4.3 Diagnosing bow type from shell emission profile

Given that the predicted shell density profile varies between wind-supported and radiation-supported bows (§ 3.3 and Fig. 5), it is worth considering whether it may be possible to use observed emission profiles to distinguish between the two.

## REFERENCES

- Arthur S. J., Hoare M. G., 2006, *ApJS*, 165, 283
- Arthur S. J., Medina S.-N. X., Henney W. J., 2016, *MNRAS*, 463, 2864
- Ballesteros-Paredes J., Hartmann L., Vázquez-Semadeni E., 1999, *ApJ*, 527, 285
- Bertoldi F., Draine B. T., 1996, *ApJ*, 458, 222
- Blaauw A., 1961, *Bull. Astron. Inst. Netherlands*, 15, 265
- Bordalo V., Telles E., 2011, *ApJ*, 735, 52
- Brott I., et al., 2011, *A&A*, 530, A115

- Canto J., Raga A. C., Wilkin F. P., 1996, *ApJ*, **469**, 729
- Cohen D. H., Wollman E. E., Leutenegger M. A., Sundqvist J. O., Fullerton A. W., Zsargó J., Owocki S. P., 2014, *MNRAS*, **439**, 908
- Courant R., Friedrichs K., 1948, *Supersonic Flow and Shock Waves*. Springer-Verlag New York
- Cox N. L. J., et al., 2012, *A&A*, **537**, A35
- Damiani F., et al., 2016, *A&A*, **591**, A74
- Dyson J. E., 1968, *Ap&SS*, **1**, 388
- Ehlerová S., Palouš J., 2005, *A&A*, **437**, 101
- Embid P., Goodman J., Majda A., 1984, *SIAM J. Sci. Stat. Comput.*, **5**, 21
- Ferrière K. M., 2001, *Reviews of Modern Physics*, **73**, 1031
- Gualandris A., Portegies Zwart S., Eggleton P. P., 2004, *MNRAS*, **350**, 615
- Gull T. R., Sofia S., 1979, *ApJ*, **230**, 782
- Hafez M., Guo W., 1999, *Computers & Fluids*, **28**, 701
- Henney W. J., Arthur S. J., 2019a, *MNRAS*
- Henney W. J., Arthur S. J., 2019b, *MNRAS*
- Henney W. J., Arthur S. J., García-Díaz M. T., 2005, *ApJ*, **627**, 813
- Hoogerwerf R., de Bruijne J. H. J., de Zeeuw P. T., 2001, *A&A*, **365**, 49
- Huenemoerder D. P., Oskinova L. M., Ignace R., Waldron W. L., Todt H., Hamaguchi K., Kitamoto S., 2012, *ApJ*, **756**, L34
- Kalberla P. M. W., Dedes L., 2008, *A&A*, **487**, 951
- Kalberla P. M. W., Kerp J., 2009, *ARA&A*, **47**, 27
- Lamers H. J. G. L. M., Cassinelli J. P., 1999, *Introduction to Stellar Winds*. Cambridge, UK: Cambridge University Press
- Lamers H. J. G. L. M., Snow T. P., Lindholm D. M., 1995, *ApJ*, **455**, 269
- Lucy L. B., 2012, *A&A*, **544**, A120
- Mac Low M.-M., van Buren D., Wood D. O. S., Churchwell E., 1991, *ApJ*, **369**, 395
- Marasco A., Fraternali F., van der Hulst J. M., Oosterloo T., 2017, *A&A*, **607**, A106
- Marcolino W. L. F., Bouret J.-C., Martins F., Hillier D. J., Lanz T., Escolano C., 2009, *A&A*, **498**, 837
- Martins F., Schaefer D., Hillier D. J., Meynadier F., Heydari-Malayeri M., Walborn N. R., 2005, *A&A*, **441**, 735
- Martins F., Mahy L., Hillier D. J., Rauw G., 2012, *A&A*, **538**, A39
- Meyer D. M.-A., Mackey J., Langer N., Gvaramadze V. V., Mignone A., Izzard R. G., Kaper L., 2014, *MNRAS*, **444**, 2754
- Meyer D. M.-A., van Marle A.-J., Kuiper R., Kley W., 2016, *MNRAS*, **459**, 1146
- Meyer D. M.-A., Mignone A., Kuiper R., Raga A. C., Kley W., 2017, *MNRAS*, **464**, 3229
- Morawetz C. S., 1956, *Communications on Pure and Applied Mathematics*, **9**, 45
- Najarro F., Hanson M. M., Puls J., 2011, *A&A*, **535**, A32
- O'Dell C. R., Ferland G. J., Peimbert M., 2017, *MNRAS*, **464**, 4835
- Oberst T. E., Parshley S. C., Nikola T., Stacey G. J., Löhr A., Lane A. P., Stark A. A., Kamenetzky J., 2011, *ApJ*, **739**, 100
- Ochsendorf B. B., Tielens A. G. G. M., 2015, *A&A*, **576**, A2
- Ochsendorf B. B., Cox N. L. J., Krijt S., Salgado F., Berné O., Bernard J. P., Kaper L., Tielens A. G. G. M., 2014a, *A&A*, **563**, A65
- Ochsendorf B. B., Verdolini S., Cox N. L. J., Berné O., Kaper L., Tielens A. G. G. M., 2014b, *A&A*, **566**, A75
- Osterbrock D. E., Ferland G. J., 2006, *Astrophysics of gaseous nebulae and active galactic nuclei*, second edn. Sausalito, CA: University Science Books
- Povich M. S., Benjamin R. A., Whitney B. A., Babler B. L., Indebetouw R., Meade M. R., Churchwell E., 2008, *ApJ*, **689**, 242
- Renzo M., et al., 2018, *arXiv*, 1804.09164
- Rodríguez-Ramírez J. C., Raga A. C., 2016, *MNRAS*, **460**, 1876
- Seddon J., Goldsmith E. L., 1999, *Intake Aerodynamics*, 2nd edn. American Institute of Aeronautics and Astronautics
- Sexton R. O., Povich M. S., Smith N., Babler B. L., Meade M. R., Rudolph A. L., 2015, *MNRAS*, **446**, 1047
- Shu F. H., Lizano S., Galli D., Cantó J., Laughlin G., 2002, *ApJ*, **580**, 969
- Smith N., Barbá R. H., Walborn N. R., 2004, *MNRAS*, **351**, 1457
- Smith N., Groh J. H., France K., McCray R., 2017, *MNRAS*, **468**, 2333
- Sternberg A., Hoffmann T. L., Pauldrach A. W. A., 2003, *ApJ*, **599**, 1333
- Tenorio-Tagle G., 1979, *A&A*, **71**, 59
- Tetzlaff N., Neuhauser R., Hohle M. M., 2011, *MNRAS*, **410**, 190
- Vink J. S., de Koter A., Lamers H. J. G. L. M., 1999, *A&A*, **350**, 181
- Vink J. S., de Koter A., Lamers H. J. G. L. M., 2000, *A&A*, **362**, 295
- Weilbacher P. M., et al., 2015, *A&A*, **582**, A114
- Wilkin F. P., 1996, *ApJ*, **459**, L31
- de Jager C., Nieuwenhuijzen H., van der Hucht K. A., 1988, *A&AS*, **72**, 259
- van Buren D., McCray R., 1988, *ApJ*, **329**, L93
- van Marle A. J., Meliani Z., Keppens R., Decin L., 2011, *ApJ*, **734**, L26

This paper has been typeset from a  $\text{\LaTeX}$  file prepared by the author.